Colloids and Surfaces A: Physicochemical and Engineering Aspects 727 (2025) 138141

Contents lists available at ScienceDirect

Colloids and Surfaces A: Physicochemical and Engineering Aspects

journal homepage: www.elsevier.com/locate/colsurfa

A novel ternary Z-scheme g-C_3N_4/CQDs/$FeVO_4$ heterojunction for photodegradation of levofloxacin via peroxymonosulfate activation

Yunuo Li [a,1], Pengda Han [a,1], Dongzhe Zhang [a], Wenzhi Zhang [a], Dong-feng Chai [a], Lijian Meng [c], Liming Bai [a,*], Ming Zhao [a,b], Guohua Dong [a,*]

[a] College of Chemistry and Chemical Engineering, Qiqihar University, Qiqihar 161006, PR China
[b] Innovation Center of Industrial Hemp for State Market Regulation, Qiqihar University, Qiqihar 161006, PR China
[c] CIETI/ISEP, Polytechnic of Porto, Rua Dr. António Bernardino de Almeida, Porto 4249-015, Portugal

HIGHLIGHTS

- A novel Z-scheme heterojunction g-C_3N_4/CQDs/$FeVO_4$ (CCF) was synthesized.
- The CCF is used to activate peroxymonosulfate to Levofloxacin (LFX) photodegradation.
- CQDs play a vital role in the enhancement of the photocatalytic performance of CCF.
- The Z-scheme transmission mechanism of CCF facilitates the photodegradation of LFX.

GRAPHICAL ABSTRACT

A novel Z-scheme g-C_3N_4/CQDs/$FeVO_4$ heterojunction photocatalyst was synthesized via microwave-assisted hydrothermal method and utilized for the photodegradation of Levofloxacin (LFX) via peroxymonosulfate activation.

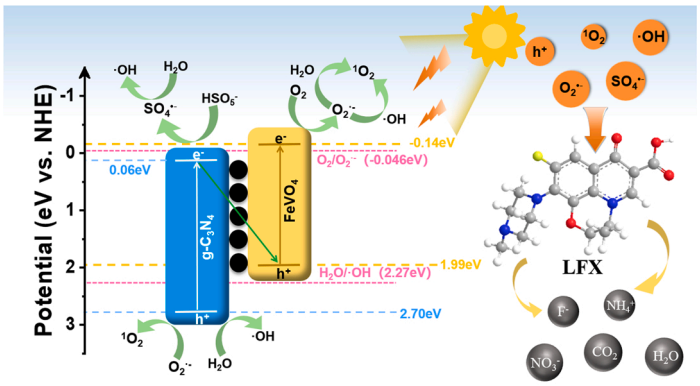

ARTICLE INFO

Keywords:
G-C_3N_4/CQDs/$FeVO_4$
Z-scheme heterojunction
Peroxymonosulfate
Levofloxacin
Photodegradation

ABSTRACT

Currently, it is still a significant challenge for photodegradation of the emerging pollutants using g-C_3N_4 (CN) due to their interior visible light responsibility and rapid recombination of e^-/h^+. Herein, a novel Z-scheme g-C_3N_4/CQDs/$FeVO_4$ (CCF) photocatalyst was synthesized by initially preparing hollow tubular g-C_3N_4/CQDs (CC) and then anchoring $FeVO_4$ on CC. The morphology, structural composition and photoelectrochemical performance of the CCF were investigated by comprehensive characterization such as FT-IR, XPS, XRD, SEM and photoelectrochemical performance tests. The CCF shows superior photodegradation capability toward LFX via activation of peroxymonosulfate (PMS), resulting in a photodegradation efficiency ~ 97.3 % in the optimal conditions. Apart from the strengthened light responsibility, improved BET specific surface area and porous texture of CCF, the improved photodegradation properties can be ascribed to the formed Z-scheme heterojunction between CC and $FeVO_4$, which can ameliorate the separation efficiency of e^-/h^+ and accelerate their

* Corresponding authors.
E-mail addresses: blm68@163.com (L. Bai), ghdong@qqhru.edu.cn (G. Dong).
[1] Yunuo Li and Pengda Han contributed to this work equally.

https://doi.org/10.1016/j.colsurfa.2025.138141
Received 23 June 2025; Received in revised form 4 August 2025; Accepted 21 August 2025
Available online 23 August 2025

transfer rate. The addition of CQDs can also serve as a channel for promoting the rapid transfer of photogenerated e^-/h^+. The photodegradation processes of LFX including generation of reactive oxygen species (ROS) and removal pathways were systematically explored by using radical capturing assays, electron spin resonance (ESR) tests and liquid chromatography-mass spectrometry (LC-MS) techniques. To sum up, this study provides an innovative method for regulating the photocatalytic activity of g-C_3N_4 via constructing Z-scheme heterostructures and incorporating CQD to degrade emerging contaminants.

1. Introduction

In the modern medical field, antibiotics are indispensable for the treatment of diseases in both humans and livestock [1]. However, their release into aquatic ecosystems has led to serious environmental pollution and ecological risks due to large-scale production, incomplete metabolism within the body and insufficient treatment methods [2,3]. Levofloxacin (LFX), a widely utilized fluoroquinolone antibiotic, is commonly found in surface water, drinking water and sewage, which raises significant concerns due to its potential risks to human health and aquatic ecosystems [4]. It is quite emergency for developing high-efficient removal technology to degrade the antibiotic contaminants [5]. In recent decades, considerable efforts have been focused on the conventional wastewater treatment (CWT) technologies including biological processes, osmosis, precipitation and adsorption due to their well-established technology and straightforward application [6,7]. However, the efficacy of CWT technologies in removing LFX effluent is often compromised owing to their high microbial toxicity together with stubborn molecular structure. On a contrary, advanced oxidation processes (AOPs) such as electrocatalysis, catalytic wet oxidation, photocatalysis and ozonation technology, hold promise for the mineralization of notorious antibiotic contaminants [8,9]. This can be mainly dominated by the highly oxidation reactive radicals including superoxide ($O_2^{\bullet-}$), hydroxyl radical (·OH) and singlet oxygen ($^1O_2$). Among these, semiconductor photocatalysis technology has captured massive research interesting for removing the persistent organic pollutants due to its efficiency, low cost and environmentally friendly [10]. In this process, reactive oxygen species (ROS) like·OH, $O_2^{\bullet-}$ or holes (h^+) are typically responsible for degradation of the contaminants. Particularly, $SO_4^{\bullet-}$ exhibits an even higher oxidation potential (~2.5–3.1 V (vs. NHE)), which has greater advantages for the degradation of pollutants [11]. Commonly, $SO_4^{\bullet-}$ is produced by activating persulfates such as peroxymonosulfate (PMS, HSO_5^-) and peroxydisulfate (PDS, $S_2O_8^{2-}$) [12]. Thus, incorporation of photocatalysis and PMS activation is a promising approach for removing recalcitrant contaminants [13,14]. Accordingly, it is quite crucial for developing photocatalyst with robust oxidative reactivity and strong visible light responsibility to efficiently activate PMS toward contaminant degradation [15,16].

Recently, graphite-like g-C_3N_4, a remarkable semiconductor photocatalyst with visible light responsibility, has attracted considerable interest across various fields (photocatalysis, electrocatalysis and sensor) because of its outstanding stability, easy synthesis, and distinctive electronic performance [17]. However, the synthesis of pure g-C_3N_4 by thermally treating the melamine, urea, or thiourea commonly suffers from undesirable agglomeration, limited photoactive sites and rapid recombination of the photogenerated charges [18,19]. Thus, it is essential for meticulously regulating the composition and structure of g-C_3N_4 to enhance its photocatalytic performance. Specifically, morphological regulation and construction of heterojunctions with other semiconductors are regarded as promising approaches for improving the photodegradation capability of g-C_3N_4. Thereby, it is extremely pivotal for choosing another catalyst with suitable conduction band (CB) potential values and valence band (VB) to form heterojunction with g-C_3N_4.

Carbon quantum dots (CQDs), a category of zero-dimensional nanomaterials featured with their small size and unique optical properties, shows diverse potential applicability [20]. CQDs, since their first discovery in 2004, has attracted significant interest for various fields including bioimaging, drug delivery, photocatalysis, and sensor technology owing to their low cytotoxicity, outstanding biocompatibility, and convenient synthesis [21–23]. Particularly, CQDs exhibit exceptionally superior photocatalytic performance toward refractory organic pollutants due to its extraordinary conductivity and semiconducting-like behavior [24,25]. Our previous work confirmed that its distinctive molecular structure and nanoscale size of CQDs can be utilized to modify the morphology of the catalyst by controlling its crystallization and growth processes, thereby enhancing the photodegradation performance of the final photocatalyst [26]. Besides, $FeVO_4$ with a bandgap of approximately 2.0–2.5 eV shows better visible-light responsibility, which is commonly applied as an accessible photocatalyst for the water splitting and the degradation of organic pollutants [27]. However, its photocatalytic performance is commonly influenced by its morphology, particle size, shape, and surface area, etc [28]. To our knowledge, $FeVO_4$ can be used as a co-catalyst for enhancing the photocatalytic performance of another catalyst by constructing a heterojunction [29,30]. Because its band structures (~-0.14 eV for CB, ~ 1.99 eV for VB) of $FeVO_4$ match well with g-C_3N_4 (0.06 eV and 2.70 eV), it can be an available selection for constructing heterojunction with g-C_3N_4 for enhancing their photocatalytic properties [31].

Herein, a novel Z-scheme g-C_3N_4/CQDs/$FeVO_4$ (CCF) heterojunction photocatalyst was developed by a two-step strategy involving the use of CQDs to induce the formation of tubular CC with impregnation coupled with annealing method and then anchoring of $FeVO_4$ on the surface of above formed CC by microwave solvothermal method. The obtained CCF was subjected to a systematic characterization with a series of techniques, including SEM, TEM, FT-IR, XRD, XPS, photoelectrochemical measurements, etc. Its photocatalytic properties were explored by photodegrading the LFX via activation of PMS under xenon lamp light source (500 W). The optimum photocatalytic performance was obtained by optimizing the photocatalytic operation parameters including dosage of applied catalysts, initial concentration of the LFX, applied concentration of PMS, aqueous pH. Finally, its potential degradation mechanism and possible degradation routes were elucidated by performing radical capture assays, ESR measurements and LC-MS analysis. Consequently, this work provides a systematical investigation on the insight about the improvement of photocatalytic property of g-C_3N_4 through combination with CQDs and $FeVO_4$.

2. Materials and methods

2.1. Chemicals and reagents

All the utilized chemicals were of analytical grade and could be used without any further treatment. More descriptions are shown in the **Text S1 (**Supplementary Material**).**

2.2. Preparation of CQDs and g-C_3N_4

The specific preparation method of CQDs and g-C_3N_4 monomer can be found in the **Text S2 (**Supplementary Material**).**

2.3. Preparation of g-C_3N_4/CQDs (CC)

The CC was prepared and optimized according to a previous method

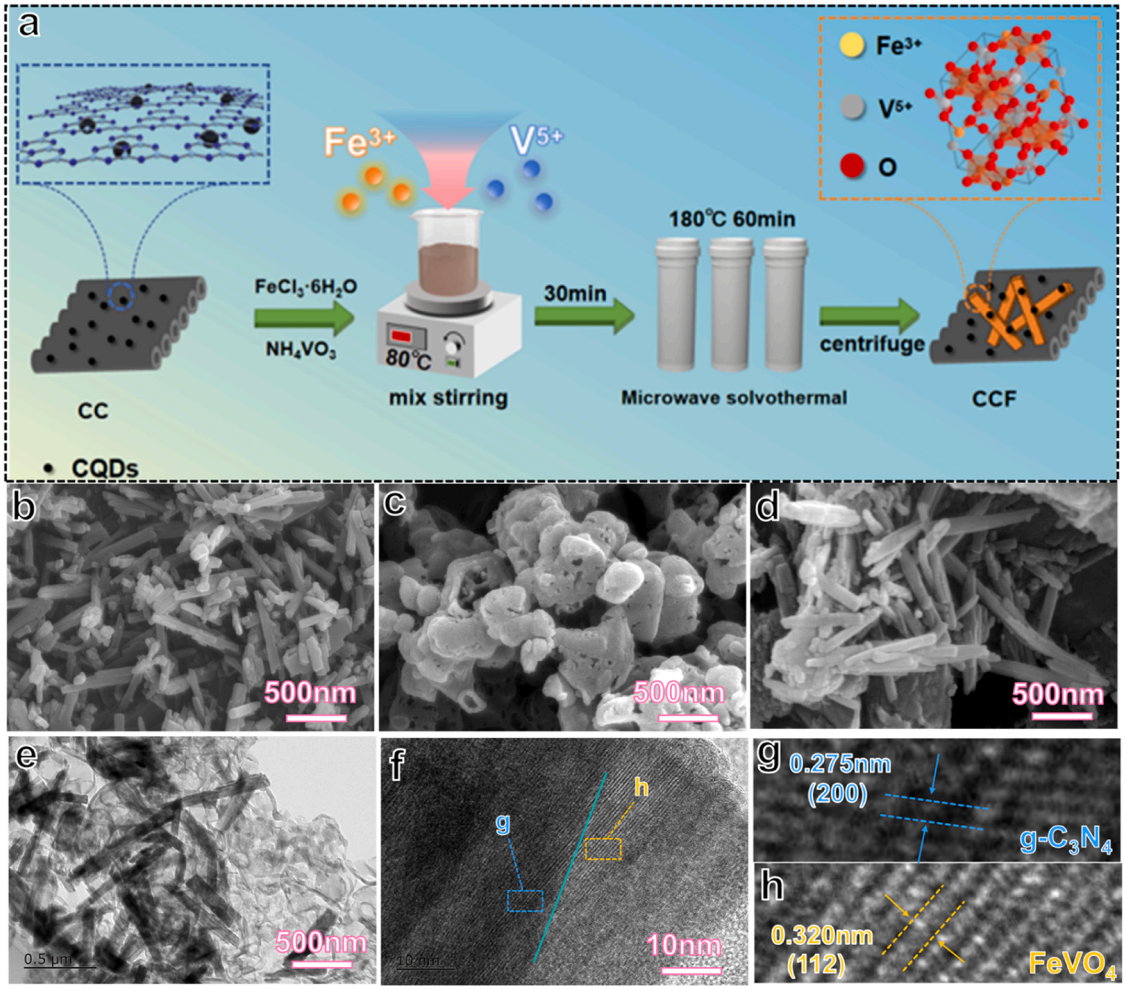

Fig. 1. (a) Schematic representation of synthesis process for CCF; (b) SEM images of $FeVO_4$; (c) CC and (d) CCF; (e) TEM image of CCF; (f-h) High-resolution transmission electron microscopy (HR-TEM) images of CCF.

[32]. Typically, 1.0 g of the generated CN precursor (**Text S2**) and 10 mL of CQDs solution (1 $g{\cdot}L^{-1}$) were mixed and a suitable amount of anhydrous ethanol was added. The mixture was placed into a round-bottom flask and then transferred to a rotary evaporator for evaporation. The collected powder-like product was calcined at 500 °C for 2 h under N_2 atmosphere to obtain CC.

2.4. Preparation of g-C_3N_4/ CQDs/$FeVO_4$ (CCF)

The g-C_3N_4/CQDs/$FeVO_4$ (CCF) was prepared utilizing a simple microwave-assisted hydrothermal method. Initially, 1.0 mmol of $FeCl_3{\cdot}6\ H_2O$ was dissolved into 50.0 mL of deionized water to form a clear orange solution (Solution A). Also, 1.0 mmol of NH_4VO_3 was dispersed into another 50.0 mL of deionized water and heated to 80 °C for preparing another solution (Solution B). After that, solution B was dropwise added to solution A under vigorous stirring, resulting in a yellow solution. Then, 1.0 g of CC was ultrasonically dispersed into the precursor solution and stirred continuously. Then, the mixture was transferred to a microwave digestion vessel and maintained at 180 °C for 60 min in a microwave reactor. The resultant precipitate was gathered and rinsed repeatedly with deionized water and absolute ethanol. Subsequently, the above-obtained precipitate was dried at 60 °C for 24 h, followed by grinding with an agate mortar to obtain CCF. Similarly, the mass ratio of the binary CC to $FeVO_4$ in the ternary CCF was optimized by varying the concentration of the precursor solution ranging from 5:1, 3:1, 3:2, 1:1–1:5 and the resulting catalysts were designated as CCF-5:1, CCF-3:1, CCF-3:2, CCF-1:1 and CCF-1:5, respectively.

2.5. Photocatalytic degradation experiment

The photodegradation experiments were performed via a photoreaction equipment (BL-GHX-V, China), which was installed with a circulation and cooling mountings to keep a temperature around 25 °C and a 500 W xenon lamp as the light source to offer continuous energy. For the photodegradation reaction, 50 mL of LFX solution was added into a quartz photoreactor and then photocatalysts were uniformly put into the LFX solution under stirring. Afterward, the solution pH was regulated to a required value. Before reaction, the suspension was maintained in a darkness environment for 30 min to attain an adsorption-desorption equilibrium. Then, PMS solution was added into the suspension and the photodegradation reaction was initiated by turning on the xenon lamp. During the degradation stage, 6 mL aliquots were withdrawn at preset time interval of 30 min and then treated with centrifugation for removing the residual photocatalyst. Concurrently, 6 mL deionized water was re-added into the reaction system for remaining a constant volume. The clear supernatant was gathered for further analysis through the UV–vis spectrophotometer (TU-1900, China) under the maximum absorption wavelength. The concentration of residual LFX was computed with a standard work curve. At last, the degradation efficiency of LFX was assessed based on the subsequent Eq. (1):

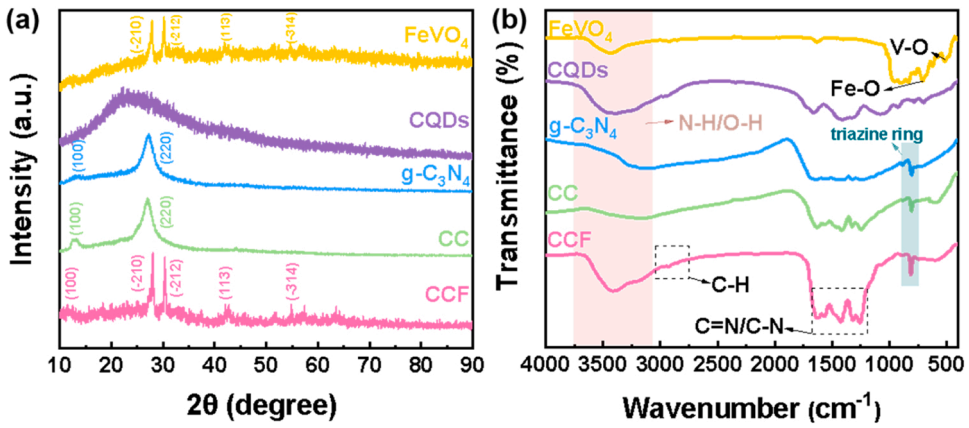

Fig. 2. (a) The XRD patterns and (b) FT-IR spectra of $FeVO_4$, CQDs, g-C_3N_4, CC and CCF.

$$\textit{LFX degradation rate}\ (\%) = [(C_0 - C_t)/C_0] \times 100 = [(A_0 - A_t)/A_0] \times 100 \quad (1)$$

where C_0 and C_t denote the concentration of LFX at time 0 and t, while A_0 and A_t refer to the absorbance intensities of the solution at time 0 and t, respectively.

Moreover, the photodegradation reaction was examined by utilizing the pseudo first-order reaction kinetic model, as listed in the Eq. (2):

$$\ln C_t/C_0 = -k\,t \quad (2)$$

where k is the apparent rate constant (min^{-1}). C_0 and C_t resemble the Eq. (1).

Notably, the photodegradation operational parameters were systematically investigated by changing the initial concentration of LFX (5 mg·L^{-1} to 40 mg·L^{-1}), the dosage of catalysts (5 mg to 40 mg), the solution pH (3, 5, 7, 9 and 11), and the utilized amounts of PMS (0.5 mL to 2.5 mL).

Moreover, the generated intermediates of LFX were explored utilizing liquid chromatography-mass spectrometry (LC-MS Ultimate, America) technology. The durability of the prepared photocatalysts were revealed via multiple recycling degradation tests with identical condition. For each cycle process, the reclaimed photocatalysts was rinsed with deionized water to remove any residual substances. Additionally, the recycled photocatalysts were investigated with SEM and FTIR for consolidating the compositional and structural changes before and after utilization.

The production of ROS during the photodegradation process was revealed with free radical trap assay. In the experiment, the adopted radical scavengers were methanol (MeOH) for trapping hydroxyl radicals (·OH) and sulfate radical ($SO_4^{\bullet-}$), isopropanol (IPA) for sacrificing ·OH, p-benzoquinone (p-BQ) for consuming the superoxide radical anion ($O_2^{\bullet-}$), L-Histidine (L-His) for scavenging the singlet oxygen ($^1O_2$), potassium iodide (KI) for detecting surface-bound free radicals, L-Ascorbic acid (L-AA) for suppressing the general radical and dimethyl Sulfoxide (DMSO) for scavenging Fe^{3+}. To further elucidating the generation of ROS, electron spin resonance (ESR) was conducted via 5, 5-dimethyl-1-pyrrolin-n-oxide (DMPO) as spin trapping agent for capturing the $O_2^{\bullet-}$, ·OH and $SO_4^{\bullet-}$ radicals. Apparently, the free radical trap assay was performed under the same conditions as the above photodegradation reaction, with the exception of the inclusion of specific scavengers.

To reveal the mineralization degree of LFX by CCF, total organic carbon (TOC) removal rate was calculated according to expression (3):

$$\textit{TOC removal rate} = [(TOC_0 - TOC)/TOC_0] \times 100\% \quad (3)$$

where, TOC_0 and TOC are the TOC values of fresh and degraded LFX solution, respectively.

All photodegradation experiments were conducted in triplicate and the gained results were statistically calculated using the analysis of variance (ANOVA) method, which are displayed as the average of the measurements with error bars representing the relative deviation from this average. The variables were analyzed based on their impact on the response at a 95 % confidence level, with a significance threshold of $p < 0.05$.

2.6. Material characterization and performance testing

More information on material characterization together with the corresponding performance testing was shown in **Text S3** and **Text S4** (Supplementary Material).

3. Results and discussion

The preparation process of the ternary CCF is exhibited in Fig. 1**a**. The process primarily consists of three steps: (i) Melamine and cyanuric acid were reacted to form the g-C_3N_4 precursor at 80 °C. The introduction of CQDs is involved in the self-polymerization reaction of the precursor, resulting in the formation of the hollow CC binary composite. (ii) The $FeCl_3{\cdot}6\ H_2O$ as the Fe source and NH_4VO_3 as the V source are introduced into the CC binary composite and thoroughly mixed through magnetic stirring. (iii) Finally, the $FeVO_4$ is embedded onto the CC composite via a microwave-assisted hydrothermal method, yielding the CCF heterojunction photocatalyst.

The morphology and microstructure of the $FeVO_4$, CC, and CCF composites were explored using the scanning electron microscopy (SEM) and transmission electron microscopy (TEM). The prepared $FeVO_4$ exhibits a nanorod structure with a cross-sectional diameter of approximately 25–50 nm (Fig. 1**b**). Fig. 1**c** presents the SEM image of CC, where the incorporation of CQDs involved in the self-polymerization process of the CN precursor, finally altering its crystallization process and yielding a hollow tubular morphology. After the formation of the ternary CCF, the nanorod $FeVO_4$ either attaches to the surface or intercalates internal the CC matrix, thereby establishing a heterojunction between the binary CC and $FeVO_4$ (Fig. 1**d**). The TEM image of CCF was shown in Fig. 1**e**, it reveals the co-existence of nanosheets and nanorods, which correspond to CC and $FeVO_4$, respectively [33]. The conversion of the hollow tubular CC to nanosheet is attributed to the ultrasonic-induced effects during the TEM preparation process. However, the CQDs within both CC and CCF are not identifiable, possibly due to their small particle size and low concentration within the binary CC and ternary CCF. The high-resolution TEM (HR-TEM) image of CCF (Fig. 1**f**) shows that the lattice spacings of about 0.275 nm aligns with the (200) lattice plane of g-C_3N_4 and 0.320 nm correspond to the (112) lattice plane of $FeVO_4$ (Figs. 1**gand** 1**h**), strongly providing the evidence for the formation of the CCF heterojunction.

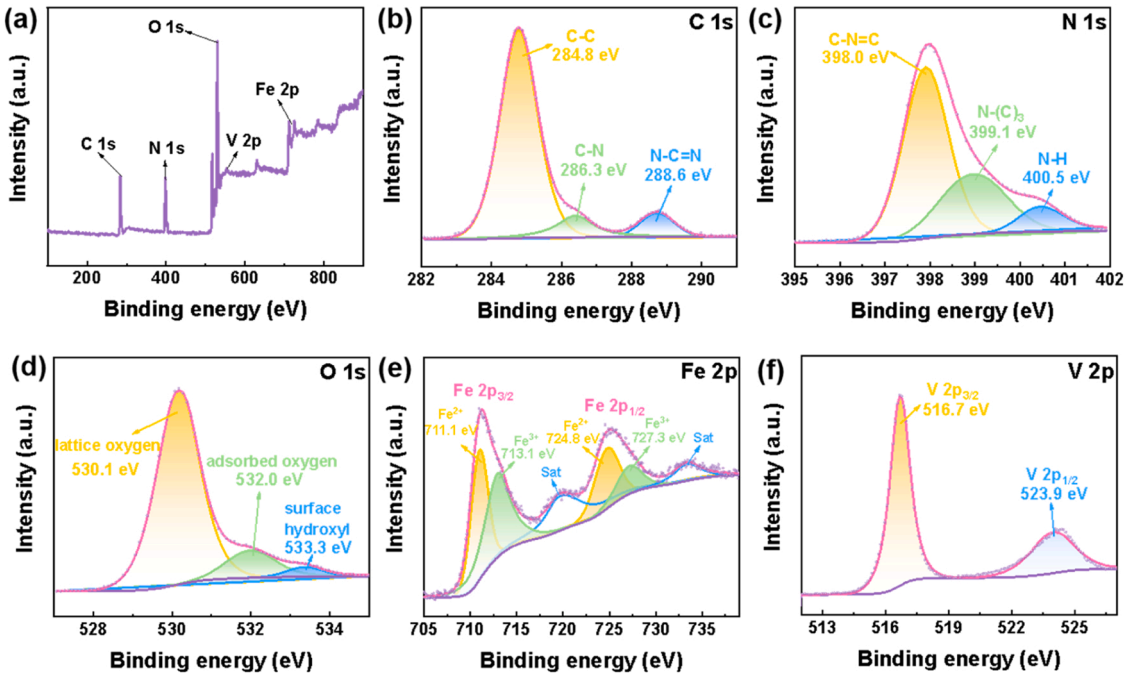

Fig. 3. (a) The survey XPS spectrum of CCF composite; The high-resolution XPS spectrum of (b) C 1 s, (c) N 1 s, (d) O 1 s, (e) Fe 2p and (f) V 2p.

Fig. 2**a** displays the XRD patterns of the obtained $FeVO_4$, CQDs, g-C_3N_4, CC, and CCF catalysts. The XRD pattern of pure g-C_3N_4 shows the distinct characteristic diffraction peaks at 13.1° and 27.0°, corresponding to (100) and (220) crystal planes, respectively [34]. The characteristic peaks of $FeVO_4$ at 27.8°, 30.1°, 41.9°, and 54.7° correspond to the (-210), (-212), (113), and (-314) crystal planes respectively, which are well coincidence with the results of standard JCPDS (JCPDS No. 71–1592). We can easily identify the characteristic peaks of $FeVO_4$ and g-C_3N_4 in the XRD pattern of CCF. However, because of the near overlap of the characteristic peak of the (220) crystal plane of g-C_3N_4 with the (-210) crystal plane of $FeVO_4$, only a single peak can be observed. The functional groups of CCF were disclosed through Fourier Transform Infrared (FT-IR) spectroscopy. The characteristic peak of g-C_3N_4 at 808 cm^{-1} is associated with the vibrations of the triazine ring units (Fig. 2**b**) [35]. Additionally, all the samples display a broad absorption peak centered approximately at 3420 cm^{-1}, which is the O-H

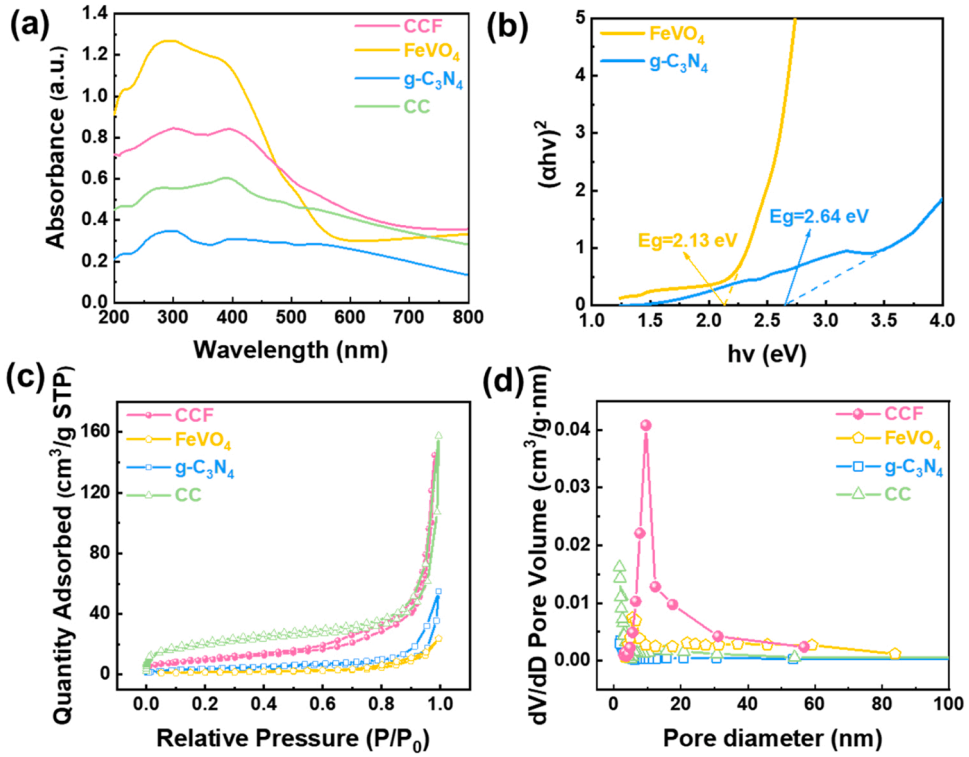

Fig. 4. (a) UV–vis DRS and (b) Tauc plots of $FeVO_4$, g-C_3N_4, CC and CCF; (c) N_2 adsorption-desorption isotherm curves and (d) pore size distribution plots of $FeVO_4$, g-C_3N_4, CC and CCF.

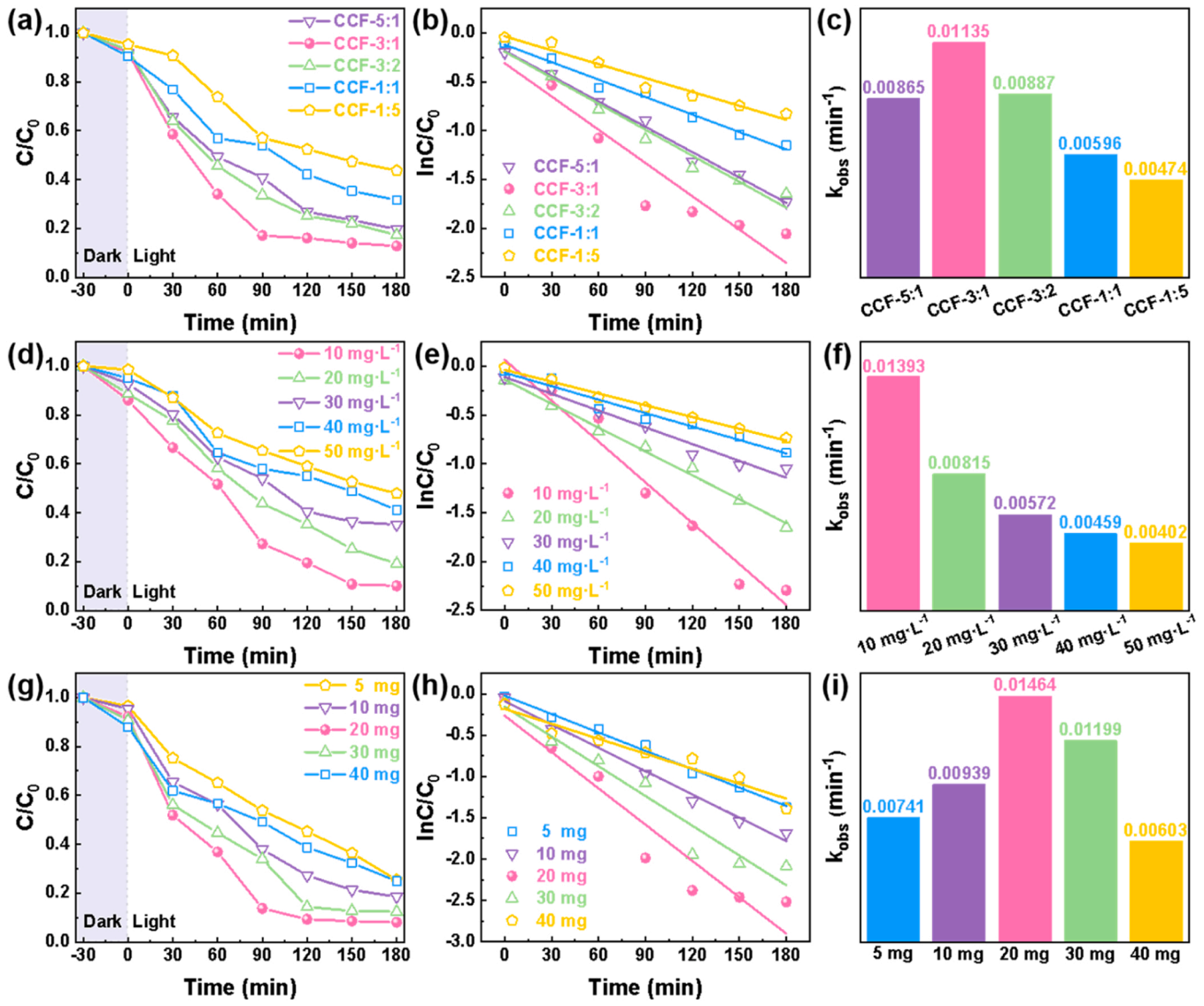

Fig. 5. (a) Optimization of adding amount of $FeVO_4$ in CCF (b) fitted photodegradation kinetic curves (c) histograms of the associated rate constants; Optimization on the photocatalytic operational parameters: (d) initial concentration of LFX (g) CCF dosage; (e, h) The corresponding first-order kinetic curves derived from Figs. 5d and 5g; (f, i) histograms of k values stem from Figs. 5e and 5h.

bonds stretching vibrations of adsorbed water molecules. Two prominent peaks of $FeVO_4$ exhibit at 708 cm^{-1} and 520 cm^{-1}, which are linked to the bending vibrations of Fe-O and V-O [36]. Furthermore, C-N/C═N heterocycles stretching vibrations lead to a series of infrared peaks in 1200 ~ 1670 cm^{-1}. For CQDs, the peaks observed at 2937 cm^{-1} and 2876 cm^{-1} are attributed to the stretching vibrations of C-H bonds. The characteristic peak at about 1068 cm^{-1} corresponds to the stretching vibrations of C-O [37]. Notably, all these peaks observed in the aforementioned samples are identifiable in the spectrum of CCF. The combined findings confirm that the CCF composite was synthesized successfully.

The XPS analysis presented in Fig. 3**a** reveals the chemical composition and surface chemical states of CCF. The survey XPS spectrum of CCF shows that the peaks are associated with C 1 s, O 1 s, N 1 s, Fe 2p, and V 2p, indicating that CCF is composed of C, O, N, Fe, and V and thereby confirming the successful preparation with CQDs, g-C_3N_4, and $FeVO_4$. Additionally, the high-resolution C 1 s XPS spectrum reveals that three characteristic peaks at binding energies of 284.8 eV, 286.3 eV, and 288.6 eV are associated with C-C, C-N, and N-C═N bonds, respectively (Fig. 3**b**). The high-resolution N 1 s XPS spectrum reveals that the peaks at 398.0 eV, 399.1 eV, and 400.5 eV are associated with C-N = C, N-$(C)_3$, and N-H bonds in Fig. 3**c**. The O 1 s XPS spectrum presents three peaks at 530.1 eV, 532.0 eV, and 533.3 eV, which are associated with lattice oxygen, adsorbed oxygen, and surface hydroxyl groups, respectively (Fig. 3**d**). In Fig. 3**e**, the peaks at 711.1 eV and 724.8 eV in the Fe 2p XPS spectrum correspond to Fe $2p_{3/2}$ and Fe $2p_{1/2}$ orbitals of Fe^{2+}. The peaks observed at 713.1 eV and 727.3 eV are attributed to the Fe $2p_{3/2}$ and Fe $2p_{1/2}$ orbitals respectively, associated with Fe^{3+} ions. The presence of satellite peaks at 719.9 eV and 733.3 eV confirms the presence of both Fe^{2+} and Fe^{3+} in the CCF heterojunction. In Fig. 3**f**, the V 2p peaks at 516.7 eV and 523.9 eV are related to the V $2p_{3/2}$ and V $2p_{1/2}$, confirming the presence of V^{5+} in the composite [28]. The XPS analysis further verifies that g-C_3N_4, CQDs, and $FeVO_4$ coexist in the CCF.

Subsequently, the physicochemical properties of the synthesized photocatalysts were systematically analyzed by UV–vis diffuse reflectance spectroscopy (UV–vis DRS). Pure $FeVO_4$ demonstrates the ability to absorb visible light, with its absorption edge occurring at ~ 550 nm (Fig. 4**a**) [36]. In contrast, CC exhibits a wide absorption spectrum extending from the UV to the visible region, lacking a distinct absorption

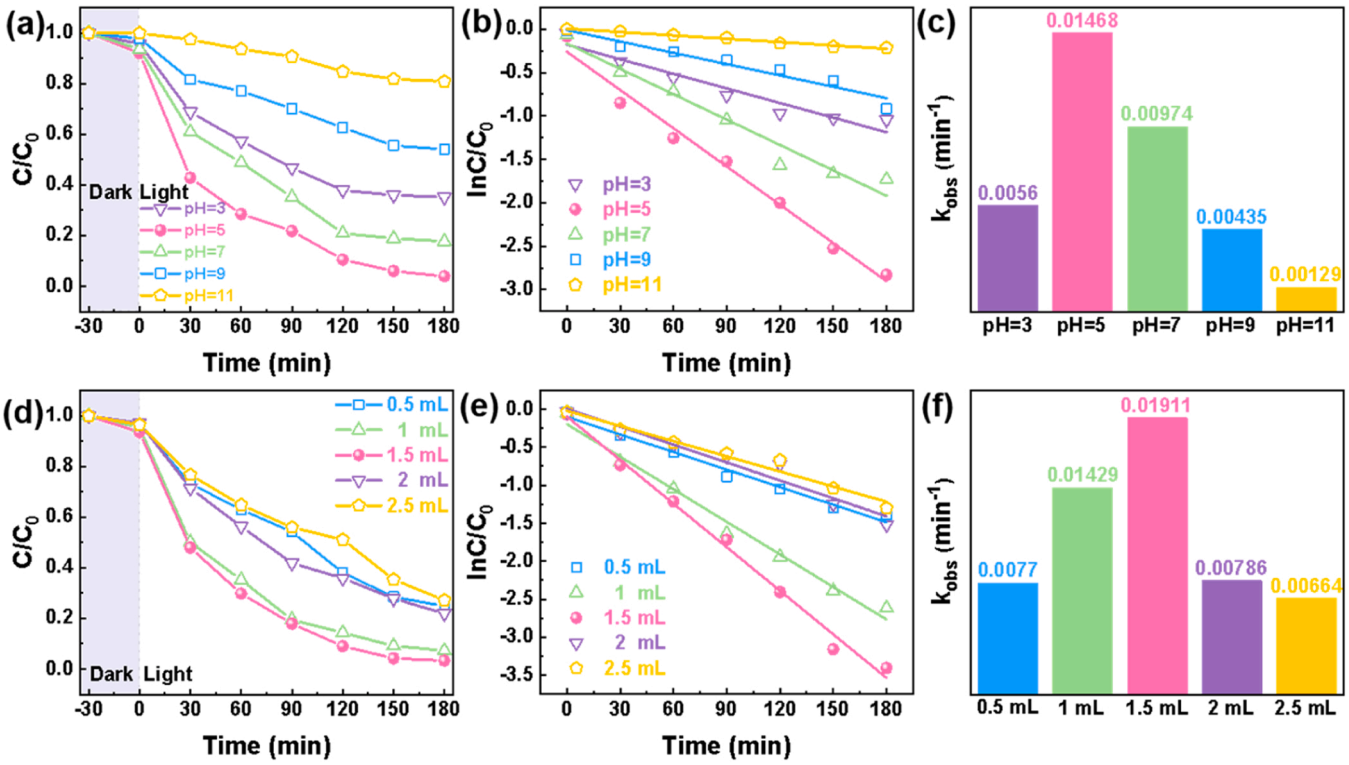

Fig. 6. Optimization on the photocatalytic operational parameters: (a) solution pH (d) PMS addition amount; (b, e) The corresponding first-order kinetic curves derived from Figs. 6a and 6d; (c, f) histograms of k values stem from Figs. 6b and 6e.

edge, which is consistent with its inherent brownish-gray characteristic. Furthermore, CCF demonstrates a broad visible light response ranging from 200 nm to 700 nm, indicating strong light absorption capability. The absorption peak of CCF exhibits an apparent red shift ~ 50 nm compared to pure g-C_3N_4, suggesting that CCF has a higher visible light utilization efficiency and a narrower bandgap. This enhancement significantly strengthens the photodegradation capability toward pollutant. The bandgaps (Eg) of the aforementioned photocatalysts were determined following the Kubelka–Munk equation ($\alpha h\upsilon = A\ (h\upsilon - E_g)^{n/2}$), where $h\upsilon$ refers to the photon energy, α stands for the absorption coefficient, Eg denotes the band gap value of semiconductor and A is the absorption, and n = 1 for direct transition and 1/2 for the indirect semiconductor. The Eg values for $FeVO_4$ and g-C_3N_4 are 2.13 eV and 2.64 eV, which were obtained by extrapolating the tangent at the band edges to the coordinate axis (Fig. 4**b**).

Subsequentially, N_2 adsorption-desorption tests were utilized to analyzing the specific surface area and pore structural properties of the synthesized samples. As presented in Fig. 4**c**, all the photocatalysts including $FeVO_4$, g-C_3N_4, CC, and CCF are classified as typical type IV isotherms with H3-type hysteresis loops according to the IUPAC classification system. This suggests the existence of mesoporous structures within these materials [38]. The specific surface areas of $FeVO_4$, g-C_3N_4, CC, and CCF were 17.36 $m^2 \cdot g^{-1}$, 22.67 $m^2 \cdot g^{-1}$, 72.18 $m^2 \cdot g^{-1}$, and 69.34 $m^2 \cdot g^{-1}$, respectively. Obviously, the CC composite photocatalyst exhibits the highest specific surface area, indicating that the integration of CQDs enhances the corresponding structural property. The larger S_{BET} of CC not only facilitates pollutant adsorption but also exposes more active sites. After incorporating CC with $FeVO_4$, the S_{BET} of the CCF composite decreased slightly compared to CC, likely due to the attachment of rod-like $FeVO_4$ on both the exterior and interior surface of the hollow CC structure. This decrease in S_{BET} indirectly confirms the formation of heterojunctions between $FeVO_4$ and g-C_3N_4, likely attributed to enhanced interfacial contact. By comparison, the $FeVO_4$ has the smallest specific surface area because of its larger particle size. According to the Barrett-Joyner-Halenda (BJH) method, the pore size distributions of $FeVO_4$, g-C_3N_4, CC, and CCF photocatalysts were 7.71 nm, 21.36 nm, 5.67 nm, and 10.34 nm, respectively, as shown in Fig. 4**d**. Although CCF does not possess the largest surface area or optimal pore structure properties, other factors can still contribute to CCF having higher photocatalytic performance. Additionally, the decrease in specific surface area and pore size indirectly confirms the formation of heterojunctions between $FeVO_4$ and g-C_3N_4 mainly due to the enhanced interfacial contact.

In view of the above investigation on the CCF by comparison with g-C_3N_4, the preparation condition of CCF was optimized by varying the mass ratio of used CC and $FeVO_4$ based on the investigation of photocatalytic degradation of LFX via PMS activation (Fig. 5**a-c**). With the increasing of the mass ratio of CC to $FeVO_4$, the photocatalytic degradation rates of LFX initially increase and then decrease. Notably, when the mass ratio of CC to $FeVO_4$ in CCF is 3:1, the generated photocatalyst (CCF-3:1) exhibits the highest degradation efficiency of 88.9 %. The photocatalytic degradation rates for catalysts with different ratios (CCF-5:1, CCF-3:2, CCF-1:1, and CCF-1:5) are 84.8 %, 86.3 %, 64.7 %, and 56.3 %, respectively. Moreover, all the photodegradation processes follow a pseudo-first-order kinetic process, with degradation rate constant (k) values of 0.00865 min^{-1} (CCF-5:1), 0.01135 min^{-1} (CCF-3:1), 0.00887 min^{-1} (CCF-3:2), 0.00596 min^{-1} (CCF-1:1), and 0.00474 min^{-1} (CCF-1:5). Based on these results, CCF-3:1 was selected as the optimal photocatalyst for further studies. The operational parameters for the photodegradation of LFX were subsequently optimized to further enhance the removal efficiency. These parameters included the initial concentration of LFX, the amount of CCF applied, the solution pH, and the volume of PMS used. In Fig. 5**d**, the concentration of LFX increase from 10 $mg \cdot L^{-1}$ to 50 $mg \cdot L^{-1}$, the removal rates decrease from 90.3 % to 56.1 %, indicating that the initial concentration significantly affects the final photocatalytic removal efficiency. There are two possible reasons: (i) higher initial pollutant concentrations may shield part of the light from entering the aqueous solution, thereby reducing

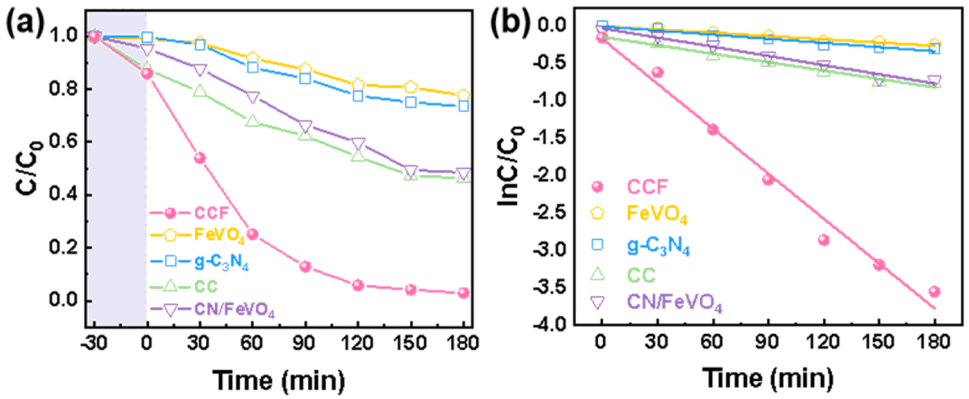

Fig. 7. (a) Photodegradation curves of LFX by $FeVO_4$, g-C_3N_4, CC, CN/$FeVO_4$ and CCF; (b) Photocatalytic degradation kinetic curves.

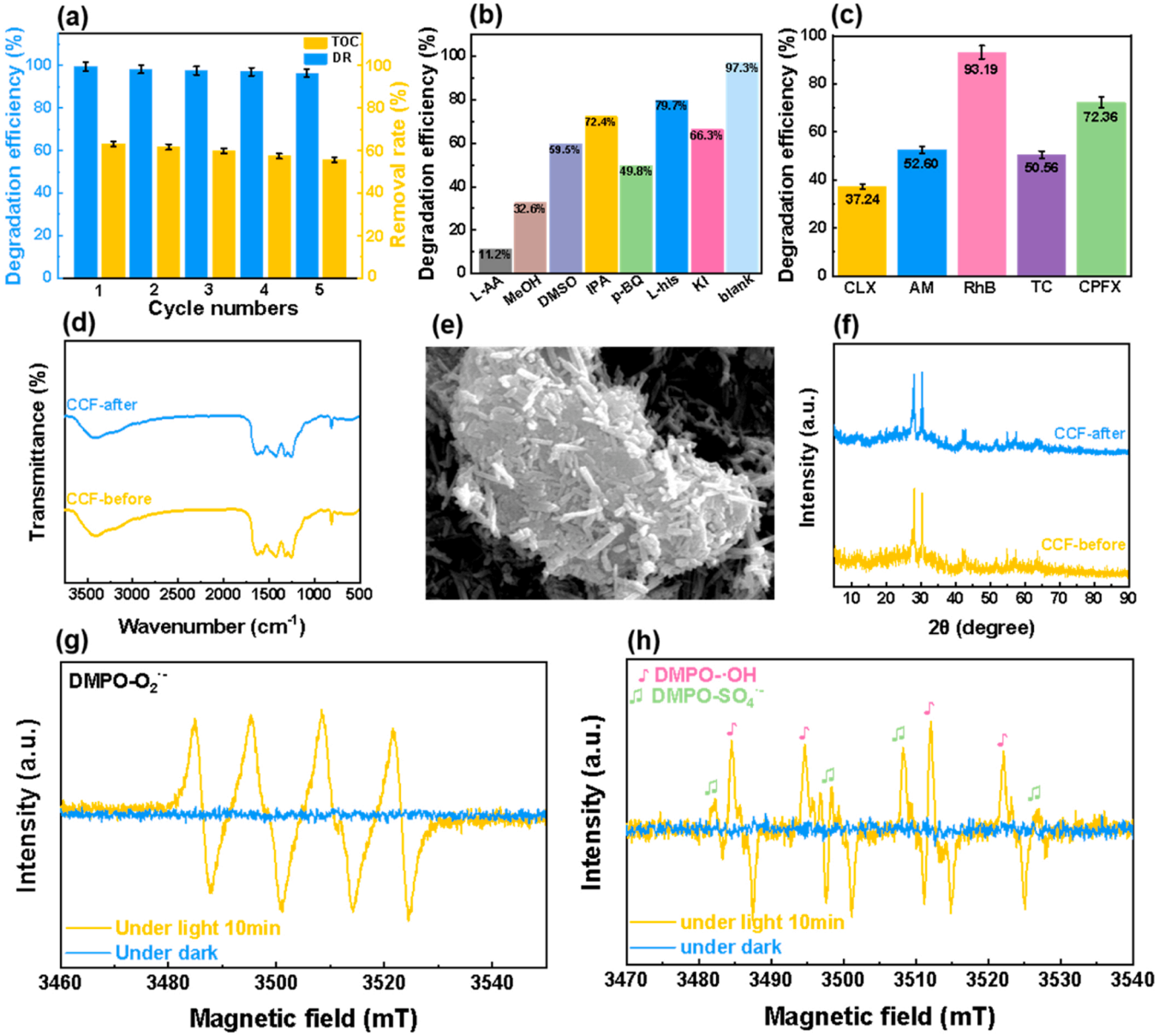

Fig. 8. (a) Cyclic photodegradation experiment toward LFX removal and the corresponding total organic carbon (TOC) removal rate; (b) Free radical capture assays; (c) universal applicability of CCF-PMS on the photodegradation toward CLX, AM, RhB, TC and CPFX; (d) XRD spectra, (e) SEM image and (f) FT-IR patterns before and after utilization; ESR signals of (g) DMPO-$O_2^{\bullet-}$ adducts and (h) DMPO- $SO_4^{\bullet-}$ and ·OH adducts in CCF-PMS system under dark and light conditions, respectively.

the visible light utilization efficiency; (ii) higher concentration of LFX solution produces more intermediate products, which can interfere both the adsorption and degradation. Therefore, 10 mg·L^{-1} of LFX was selected for subsequent experiments. The k values for the above photodegradation (Fig. 5**e-f**) are 0.01393 min^{-1} (10 mg·L^{-1}), 0.00815 min^{-1} (20 mg·L^{-1}), 0.00572 min^{-1} (30 mg·L^{-1}), 0.00459 min^{-1} (40 mg·L^{-1}), and 0.00402 min^{-1} (50 mg·L^{-1}), respectively. Additionally, in Fig. 5**g**, the optimal dosage of the photocatalyst is 20 mg, achieving the maximum photocatalytic degradation rate of 90.9 %. Lower dosages minor 20 mg results in underutilization of light, as some of the light passed through the solution without participation on the reaction. Conversely, an excessive amount of photocatalyst exceeding 40 mg leads to light obstruction and scattering phenomena. The pseudo-first-order kinetic model also adequately simulates the process of photodegradation of LFX, with k values of 0.00741 min^{-1} (5 mg), 0.00939 min^{-1} (10 mg), 0.01464 min^{-1} (20 mg), 0.01199 min^{-1} (30 mg), and 0.00603 min^{-1} (40 mg), respectively (Fig. 5**h-i**).

The impact of aqueous pH on the photocatalytic degradation rate of LFX (20 mg·L^{-1}) was investigated using CCF (20 mg) to activate PMS under light. When the pH increases from 3 to 5, the photocatalytic removal rate significantly increases from 61.3 % to 95.8 % (Fig. 6**a**), with k values increasing from 0.0056 to 0.01468 min^{-1} (Fig. 6**b**). However, as the pH continue to rise to 7, 9, and 11, the removal rates by CCF show a marked decreasing trend, dropping to 81.6 %, 42.5 %, and 17.7 %, respectively, with k values significantly decreasing to 0.00974 min^{-1}, 0.00435 min^{-1}, and 0.00129 min^{-1}. It is clear that weakly acidic condition favors for the removal of LFX, while strong acidic and basic conditions inhibit the photocatalytic reaction. This observed phenomenon can be explained as follows: when the pH = 3, PMS mainly exists as H_2SO_5, which is unfavorable for generating highly active sulfate radical ($SO_4^{\bullet-}$). In alkaline conditions, LFX primarily exists in its anionic form (LFX^-), while PMS mainly exists as HSO_5^- and SO_5^{2-}. This results in electrostatic repulsion between LFX and PMS, significantly hindering the breakdown of LFX. Additionally, in strongly acidic condition, the protonation-deprotonation equilibrium of $O_2^{\bullet-}$ is disrupted, resulting in $O_2^{\bullet-}$ consumption [39,40]. Conversely, at elevated pH levels, the $SO_4^{\bullet-}$ produced from PMS activation reacts with OH^-, converting into •OH, which reduces oxidation capability. Furthermore, a key degradation mechanism of LFX involves the breaking of the piperazine ring. Under weakly acidic conditions, the cationic form of LFX is more prone to undergo reactions that open the piperazine ring. Thus, the degradation rate is more significant in the weakly acidic condition. Consequently, the highest degradation rate approximately 95.8 % can be gained at the optimal pH ~ 5. Commonly, the concentration levels of PMS determine the amount of ROS generated. 1 mol·L^{-1} of PMS was selected as the stock solution in the photodegradation process. In Fig. 6**d**, with the dosages of added PMS increasing from 0.5 mL to 1.5 mL, the photocatalytic degradation rate of LFX significantly increase from 72.9 % to 97.3 %, and meanwhile the k values show a gradual improvement from 0.0077 min^{-1} to 0.01911 min^{-1} (Fig. 6**e**), confirming that an appropriate amount of PMS can promote the photodegradation of LFX. However, with the continuous increase of the PMS dosages to 2 mL and 2.5 mL, the photodegradation rates of LFX are 74.3 % and 70.2 % respectively, finally leading to k values of 0.00786 min^{-1} and 0.00664 min^{-1}. This can be reasonably interpreted by the fact that a small amount of PMS leads to insufficient contact between ROS and LFX. Furthermore, an overabundance of PMS in the degradation system interacts with produced electrons and radicals (like $SO_4^{\bullet-}$), transforming into a less active radical (such as $SO_5^{\bullet-}$). This process results in unfavorable competitive reactions within the degradation system. Additionally, excess $SO_4^{\bullet-}$ may lead to self-quenching, thereby reducing oxidation capability [41]. To sum up, the optimal dosage of 1 mol·L^{-1} PMS for LFX degradation is determined to be 1.5 mL.

The photocatalytic activity of CCF toward LFX degradation was evaluated by activating PMS under the optimal operation conditions confirmed in above investigations. In Fig. 7**a**, the photodegradation toward LFX by pure g-C_3N_4 and $FeVO_4$ are relatively low with removal rates of 22.3 % and 26.4 % respectively, indicating their limited photocatalytic activity. For the binary composites, CC exhibits a stronger degradation rate up to 51.5 %, which can be attributed to its unique hollow morphology and enhanced conductivity for the photogenerated charges. This structure offers an enhanced specific surface area along with additional active sites, consequently improving the photocatalytic degradation efficiency. The photocatalytic degradation efficiency of CN/$FeVO_4$ is relatively low at 53.6 %, suggesting the creation of a heterojunction between g-C_3N_4 and $FeVO_4$. The CCF ternary system shows the highest degradation rate reaching approximately 97.3 %. The higher photocatalytic activity of CCF may be explained to several factors: (i) the creation of a Z-scheme heterojunction enhances the separation of photogenerated electron-hole (e^-/h^+) pairs; (ii) CQDs accelerate the separation of photogenerated e^-/h^+ pairs; (iii) the greater specific surface area provides abundant reactive sites for the adsorption and catalysis reaction. Additionally, the photodegradation kinetics of LFX (Fig. 7**b**) reveals that all the photocatalytic reactions follow a pseudo-first-order kinetic. Among these catalysts, CCF possesses the highest k up to 0.02002 min^{-1}, which is 13.8, 10.8, 5.34, and 4.88 times higher than those of $FeVO_4$ (0.00145 min^{-1}), g-C_3N_4 (0.00185 min^{-1}), CN/$FeVO_4$ (0.00375 min^{-1}), and CC (0.00410 min^{-1}), respectively. By comparison with the previously reported g-C_3N_4-based photocatalysts (Table S1), CCF still exhibits higher advantages in photodegradation of pollutant.

The reusability of the photocatalysts is extremely crucial for the practical application. Thus, the stability of the CCF was evaluated by repeatedly recycling LFX photodegradation for five cycles. After each of the cycle experiments, the recycled photocatalyst was washed and dried before the next utilization. In Fig. 8**a**, the degradation efficiency of LFX remains at 96.4 % after five cycles, decreasing by only about 3.6 %, indicating that the CCF photocatalyst possesses outstanding stability and reusability. The reduction of the photodegradation rate could be attributed to the mass loss of the photocatalyst during recovery and the blocking of the reactive sites by the formed intermediates [42]. Meanwhile, the mineralization degree of the LFX was assessed by monitoring the TOC removal rate during the cycle degradation assay. As illustrated in Fig. 8**a**, in the first cycle of the photodegradation experiment, the CCF-PMS system achieves a notable TOC removal rate up to 63.2 % toward LFX. After five consecutive runs, the TOC removal rate slightly drops to 55.8 %, suggesting that CCF has outstanding ability to mineralize LFX into inorganic substances. Moreover, during the initial run, the fact that the TOC removal rate (63.2 %) is lower than the photodegradation efficiency (99.6 %) can be ascribed to the generation of intermediate products. The radical capture assays were performed for investigating the ROS by adding isopropanol (IPA) for capturing ·OH, methanol (MeOH) for trapping ·OH and $SO_4^{\bullet-}$, L-Ascorbic acid (L-AA) for suppressing the general radical, p-benzoquinone (p-BQ) for consuming $O_2^{\bullet-}$, L-histidine (L-his) for scavenging $^1O_2$, potassium iodide (KI) for eliminating surface-bound free radicals and dimethyl sulfoxide (DMSO) for scavenging Fe^{3+}, respectively. As shown in Fig. 8**b**, without adding any scavengers, the removal rate of LFX in the CCF-PMS system can reach 97.3 %. After adding IPA into the degradation system, the degradation efficiency decreases to 72.4 %. However, with the introduction of MeOH and L-AA solutions, the degradation efficiency declines to 32.6 % and 11.2 %, respectively. Thus, it can be reasonably inferred that in the CCF-PMS system for the photodegradation of LFX, $SO_4^{\bullet-}$ is the primary reactive oxygen species (ROS), while ·OH is the subordinate ROS. Upon adding L-his to the solution, the degradation efficiency decreases slightly, indicating that $^1O_2$ makes the least contribution to photodegradation of LFX [26]. The addition of p-BQ significantly inhibits the degradation efficiency, demonstrating that $O_2^{\bullet-}$ is among the primary radicals involved in the degradation process. The addition of DMSO indicates that the high-valent Fe^{3+} also plays a certain role in the degradation process. In summary, $SO_4^{\bullet-}$, $O_2^{\bullet-}$, ·OH, and $^1O_2$ radicals all participate in the photodegradation of LFX, the sequence of the action of

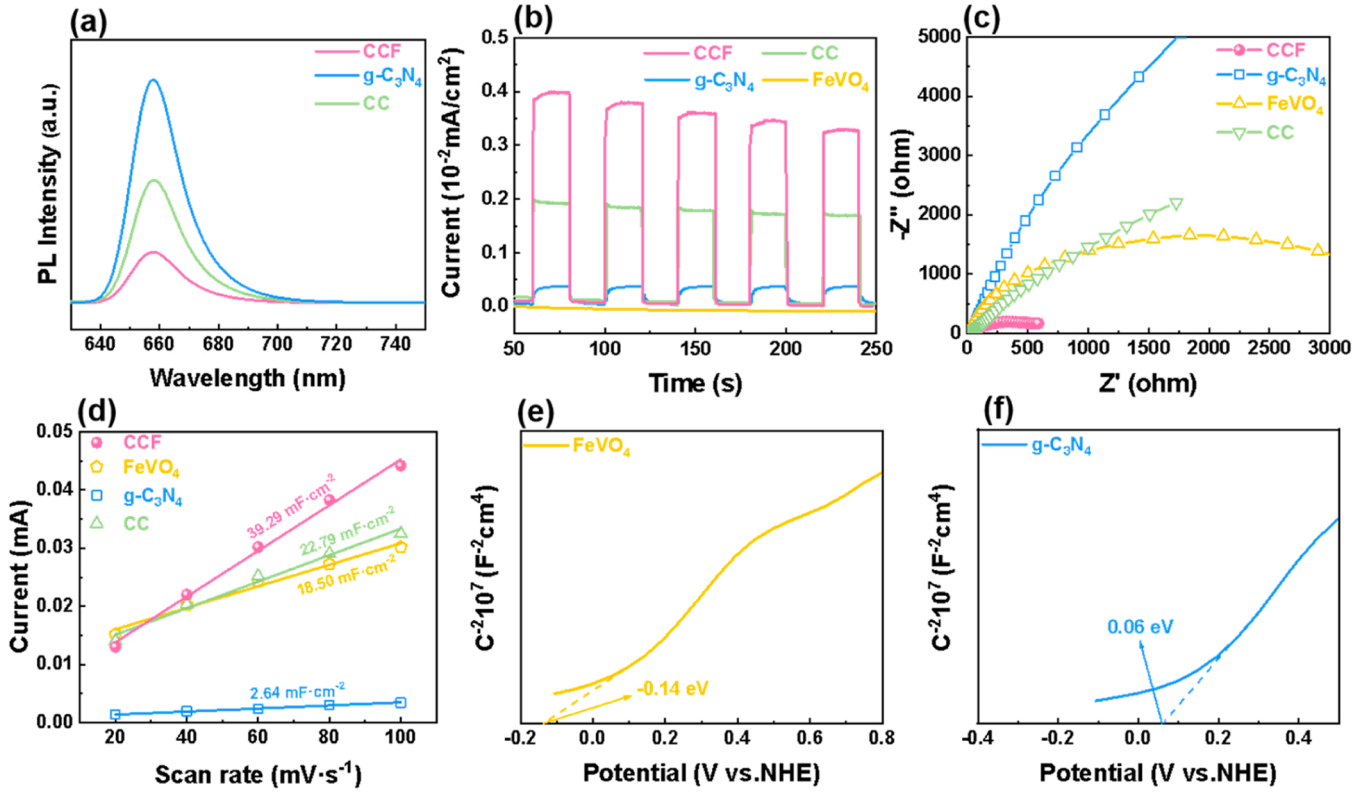

Fig. 9. (a) The PL spectra of g-C_3N_4, CC and CCF; (b) Transient photocurrent response spectra;(c) EIS spectra and (d) ECSA tests of $FeVO_4$, g-C_3N_4, CC and CCF catalysts; The Mott-Schottky curves of (e) $FeVO_4$ and (f) g-C_3N_4.

LFX photodegradation is $SO_4^{\bullet-} > O_2^{\bullet-} > \cdot OH > {}^1O_2$. Additionally, when L-AA is involved into the system, almost no photodegradation reaction occurs, indicating that ROS can be considered to originate from the CCF-PMS system. Upon adding KI, the degradation efficiency drops by roughly 31.0 %, which indicates that radicals participating in the photodegradation process are also generated on the surface of the CCF binding layer. Overall, the photodegradation of LFX through the CCF-PMS system is an intricate catalytic reaction that encompasses various radicals. To further investigate the practical applicability of the prepared CCF, the photodegradation efficiencies of various contaminants including tetracycline (TC), rhodamine B (RhB), aureomycin (AM), cefalexin (CLX) and ciprofloxacin (CPFX) by CCF-PMS were collected and evaluated. As shown in Fig.8**c**, with an identical irradiation time of 180 min, the obtained degradation efficiencies of CLX, AM, RhB, TC and CPFX are 37.24 %, 52.60 %, 93.19 %, 50.56 % and 72.36 %, respectively, revealing that the prepared CCF possesses remarkable universality toward the photocatalytic removal of a variety of refractory contaminants. The difference of the degradation efficiencies for varied target pollutants can mainly be related to the intrinsic selectivity of the synthesized photocatalyst and the complexity of the pollutants. To further assess the stability of the photocatalyst after recycling, the XRD, SEM and FT-IR of the used CCF were collected. As illustrated in Fig. 8**d-f**, the used CCF reveals negligible changes before and after the five cycles, further proving that CCF has excellent stability and reusability.

Furthermore, ESR tests provided confirmation of the presence of the primary ROS ($O_2^{\bullet-}$, $SO_4^{\bullet-}$, and •OH), in which DMPO was used as the spin-trapping agent. The CCF system (with no PMS) exhibits four distinct and consistent peaks with the intensity ratio of 1:1:1:1 under light irradiation, suggesting the formation of the DMPO-$O_2^{\bullet-}$ adduct (Fig. 8**g**). No ESR signals were observed under dark as the catalyst does not generate any radicals without the light [43]. Upon introducing PMS into the CCF system, the peaks exhibit significant differences compared to the previously identified ESR peaks (Fig. 8**h**). This suggests the simultaneous generation of •OH and $SO_4^{\bullet-}$ radicals in the CCF-PMS system under light irradiation. Therefore, the ESR test results further confirm that $O_2^{\bullet-}$, •OH, and $SO_4^{\bullet-}$ are the main ROS responsible for the photodegradation in the CCF-PMS system.

Photoluminescence (PL) testing serves as an efficient method to clarify the separation and recombination mechanisms of photogenerated e^-/h^+. In general, a lower PL intensity in heterojunction composites indicates that the separation of e^-/h^+ pairs is more effective and recombination is less, finally resulting in better photocatalytic performance. In Fig. 9**a**, in contrast to pure g-C_3N_4 and CC, CCF exhibits the smallest PL emission peak intensity, manifesting that the recombination rate of photogenerated e^-/h^+ in the composite is significantly reduced and CCF possesses higher photocatalytic activity than that of others [43]. This can be mainly ascribed to the effective enhancement of charge separation and accelerated migration of photogenerated carriers within the nanocomposite structure [44]. Furthermore, the well-separated and rarely recombined e^-/h^+ pairs lead to an enhanced transient photocurrent response. As illustrated in Fig. 9**b**, all the photocatalysts show negligible transient photocurrent in the absence of light. However, under illumination, the photocurrent density increases quickly and subsequently levels off a specific value, indicating the high photosensitivity of these samples [45]. By comparison, the CCF has the highest transient photocurrent under illumination, confirming its outstanding photosensitivity, rapid charge separation/transfer and effective inhibition of recombination. From the EIS curve in Fig. 9**c**, we can observe that the radius of the arc of the CCF complex is significantly smaller than that of the other three catalysts, demonstrating that the CCF possesses smaller charges transfer resistance. The lower charge transfer resistance of CCF can result in effective enhancement of the interfacial charge transfer ability, finally leading to decline for the charges recombination.

Generally speaking, photocatalytic performance of the

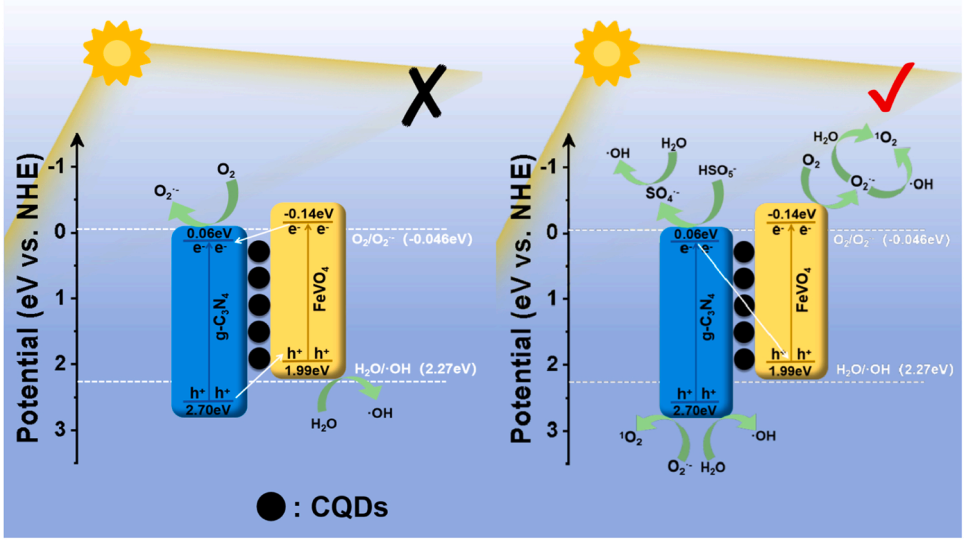

Fig. 10. Schematically illustration on the possible photodegradation mechanism of LFX by CCF-PMS system.

photocatalysts is mainly depended on the number of reactive sites, which is closely correlated with ECSA of the catalyst. By investigating the CV curves of the developed photocatalysts in non-Faraday regions, the C_{DL} for $FeVO_4$, g-C_3N_4, CC, and CCF was calculated as 18.50 mF·cm^{-2}, 2.64 mF·cm^{-2}, 22.79 mF·cm^{-2}, and 39.29 mF·cm^{-2}, respectively (Fig. 9**d**). After further calculation with the equation described in **Text S4** (Supplementary Material), the ECSA values of $FeVO_4$, g-C_3N_4, CC, and CCF are 0.463 cm^2, 0.066 cm^2, 0.569 cm^2, and 0.982 cm^2, respectively. Clearly, CCF has the largest ECSA value of 0.982, confirming that CCF can provide the most reaction active sites for pollutant adsorption and photodegradation throughout the photocatalytic procedure. The physicochemical properties of the semiconductors were further elucidated through Mott-Schottky measurements, shedding light on the potential photocatalytic degradation mechanism. As shown in Fig. 9**e-f,** both of the g-C_3N_4 and $FeVO_4$ are n-type semiconductors because of their positive slopes. By extrapolating the linear portions to intersect with the x-axis, the flat band potentials (E_{fb}) for g-C_3N_4 and $FeVO_4$ were determined to be 0.06 eV (vs. NHE) and −0.14 eV (vs. NHE). It is widely recognized that the CB value of n-type semiconductors is roughly equivalent to the E_{fb}. Therefore, the CB positions (E_{CB}) for g-C_3N_4 and $FeVO_4$ are 0.06 eV (vs. NHE) and −0.14 eV (vs. NHE). Considering the previously calculated bandgap (Eg) values of 2.64 eV for g-C_3N_4 and 2.13 eV for $FeVO_4$, the valence band (E_{VB}) positions for g-C_3N_4 and $FeVO_4$ can be obtained by the formula $E_{VB} = E_{fb} + Eg$. Accordingly, the E_{VB} values are 2.70 eV for g-C_3N_4 and 1.99 eV for $FeVO_4$.

During the degradation process, photogenerated electrons (e^-) in $FeVO_4$ and g-C_3N_4 are excited from the VB to the CB, while holes (h^+) remain in the VB. Defect energy levels can enhance the enrichment of e^- and influence their transfer direction. The E_{CB} of $FeVO_4$ (-0.14 eV) is more negative than that of g-C_3N_4 (0.06 eV), and the E_{VB} of g-C_3N_4 (2.70 eV) is higher than that of $FeVO_4$ (2.27 eV). Assuming the photocatalytic degradation mechanism of CCF follows Type II, photogenerated e^- in the CB of $FeVO_4$ would transfer to the CB of g-C_3N_4, while h^+ in the VB of g-C_3N_4 would transfer to the VB of $FeVO_4$. In this scenario, the generated e^- react with O_2 to form $O_2^{\bullet-}$, and the generated h^+ react with H_2O to produce ·OH. This pathway could not take place, because the CB potential of g-C_3N_4 (0.06 eV) is more positive than that of the $O_2/O_2^{\bullet-}$(-0.046 eV). This contradicts the presence of active substances ($O_2^{\bullet-}$) identified in the free radical scavenging test results. Therefore, it can be speculated that the Z-scheme is a suitable mechanism for CCF in photocatalytic degradation of LFX. Based on this situation, we have revised the contents for confirming the Z-scheme mechanism of CCF. As shown in Fig. 10, upon light excitation of CCF (Eq. (4)), electrons in the VB of g-C_3N_4 and $FeVO_4$ are initially stimulated to their respective CB. The electrons in the CB of g-C_3N_4 then transfer directly to the VB of $FeVO_4$, where they rapidly combine with holes in the VB of $FeVO_4$, thereby enhancing the efficiency of photogenerated charge separation. In this process, the excellent conductivity of CQDs in CCF acts as a charge transfer way, facilitating the rapid movement of photogenerated electrons and thus improving the photocatalytic efficiency of CCF [26]. Given the more negative CB potential of $FeVO_4$ (-0.14 eV vs NHE) relative to that of $O_2/O_2^{\bullet-}$ (-0.046 eV vs NHE), the photogenerated electrons can react with O_2 to form $O_2^{\bullet-}$(Eq. (5)). Compared to the $H_2O/·OH$ (2.27 eV vs NHE), the VB of g-C_3N_4 (2.70 eV vs NHE) exhibits a more positive potential. The abundant holes in the VB of g-C_3N_4 can readily oxidize H_2O, leading to the production of ·OH (Eq. (6)). These finding suggest that the effective creation of the CCF Z-scheme heterojunction facilitates charge separation and transfer, boosts redox activity, leading to an enhancement in photocatalytic efficiency [46].

Moreover, the activation of PMS within this system plays a surprisingly significant role in further enhancing the photodegradation rate of LFX. Initially, the photogenerated electrons in the CB of g-C_3N_4 are trapped by PMS, leading to formation of $SO_4^{\bullet-}$ (Eq. (7)), and some of the $SO_4^{\bullet-}$ then reacts with H_2O to generate ·OH (Eq. (8)). Additionally, based on the XPS spectra showing the presence of Fe^{2+} and Fe^{3+} in CCF, it is reasonable to infer that Fe^{3+} can be reduced to Fe^{2+} by $O_2^{\bullet-}$ (Eq. (9)), and can also react with HSO_5^- to produce Fe^{2+} and $SO_5^{\bullet-}$ (Eq. (10)). Subsequently, the generated Fe^{2+} can further react with HSO_5^- to oxidize back to Fe^{3+}, ultimately producing $SO_4^{\bullet-}$(Eq. (11)), thereby achieving mutual conversion between Fe^{2+} and Fe^{3+}, and triggering the redox cycle of Fe^{3+} and Fe^{2+}, which is beneficial for the continuous and quick generation of a large number of radicals. Additionally, radical trapping experiments reveals the presence of non-radical $^1O_2$ in the CCF-PMS system. In fact, $O_2^{\bullet-}$ can react with h^+, H_2O, and ·OH to produce $^1O_2$ (Eqs. (12–14)). Finally, with the collaboration of $SO_4^{\bullet-}$, $O_2^{\bullet-}$, ·OH, h^+, and $^1O_2$, LFX is broken down into small inorganic molecules CO_2 and H_2O in the CCF-PMS system (Eq. (15)). Thus, the charge separation in the Z-scheme CCF heterojunction photocatalyst provides a large number of photogenerated electrons for activating PMS. This process facilitates the redox cycling between Fe^{3+} and Fe^{2+}, and consequently enabling rapid PMS activation. At the same time, it reduces the recombination of photogenerated e^-/h^+ pairs, which in turn boosts the photodegradation efficiency.

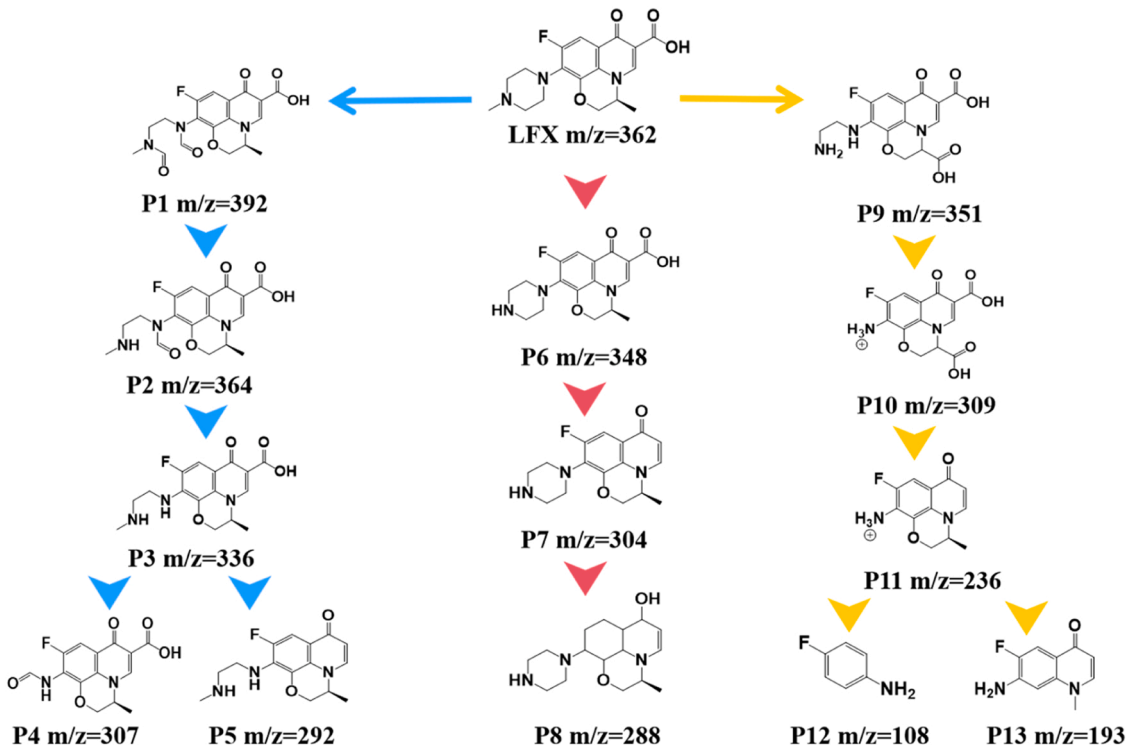

Fig. 11. The potential pathways of photodegradation for LFX.

$$CCF + hv \rightarrow e^- + h^+ \quad (4)$$

$$e^- + O_2 \rightarrow O_2^{\bullet-} \quad (5)$$

$$h^+ + H_2O \rightarrow \cdot OH + H^+ \quad (6)$$

$$e^- + HSO_5^- \rightarrow SO_4^{\bullet-} + OH^- \quad (7)$$

$$SO_4^{\bullet-} + H_2O \rightarrow SO_4^{2-} + \cdot OH + H^+ \quad (8)$$

$$Fe^{3+} + O_2^{\bullet-} \rightarrow Fe^{2+} + O_2 \quad (9)$$

$$Fe^{3+} + HSO_5^- \rightarrow Fe^{2+} + SO_5^{\bullet-} + H^+ \quad (10)$$

$$Fe^{2+} + HSO_5^- \rightarrow Fe^{3+} + SO_4^{\bullet-} + OH^- \quad (11)$$

$$O_2^{\bullet-} + h^+ \rightarrow {}^1O_2 \quad (12)$$

$$2O_2^{\bullet-} + 2H_2O \rightarrow {}^1O_2 + H_2O_2 + 2OH^- \quad (13)$$

$$O_2^{\bullet-} + \cdot OH \rightarrow {}^1O_2 + OH^- \quad (14)$$

$$SO_4^{\bullet-} / O_2^{\bullet-} / \cdot OH / h^+ / {}^1O_2 + LFX \rightarrow \text{degradation products} \quad (15)$$

To further investigate the photodegradation process of LFX by CCF through PMS activation, three potential pathways toward LFX photodegradation were reasonably inferred by leveraging the known photodegradation intermediates with LC-MS technology [47]. Table S2 presents the details of potential degradation products and Fig. S1 shows the obtained mass spectra of intermediates. As presented in Fig. 11, the first pathway starts with the epoxidation of the piperazine ring, yielding P1 ($m/z = 392$), then the removal of a carbonyl group to generate P2 ($m/z = 364$) and P3($m/z = 336$). The removal of an acetamide methyl group and carboxyl group occurs to obtain P4 ($m/z = 307$) and P5 ($m/z = 292$). The second pathway involves demethylation of LFX to produce P6 ($m/z = 348$), followed by decarboxylation to form P7 ($m/z = 304$) and defluorination to produce P8 ($m/z = 288$). The third pathway begins with the ring-opening reaction of the piperazine ring to form P9 ($m/z = 351$), followed by the elimination of a methylacetamide group and decarboxylation to yield P10 ($m/z = 309$) and P11 ($m/z = 236$). Finally, P4, P5, P8, P12, and P13 are degraded into CO_2, H_2O, NO_3^-, NH_4^+, and F^-, respectively [48–50].

4. Conclusion

In summary, a novel Z-scheme ternary g-C_3N_4/CQDs/$FeVO_4$ (CCF) composite photocatalyst was synthesized by initially preparing hollow tubular g-C_3N_4/CQDs (CC) and then anchoring $FeVO_4$ on CC. The CCF photocatalyst possesses distinctive tubular morphology, enhanced light response capability and higher S_{BET} than those of neat g-C_3N_4. Under the optimal conditions, the CCF shows a higher the photodegradation efficiency toward LFX reaching 97.3 % compared to other monomers and binary photocatalysts, which was 4.36 times of pure g-C_3N_4 (22.3 %). In addition, CCF also shows superior durability after performing 5 cycles photodegradation and can effectively mineralize the LFX into inorganic substance with TOC removal rate ~ 63.2 %. This can be principally because of the construction of Z-scheme heterojunction and CQDs as carriers transport pathway, both of which can improve the separation efficiency, accelerate the charges transport rate together with reduce the recombination of the photogenerated charges. Free radical capture experiments coupled with the ESR measurements reveals that the $SO_4^{\bullet-}$, $O_2^{\bullet-}$, ·OH, $^1O_2$ are the ROS responsible for the photodegradation of LFX. The identified degradation intermediates by LC-MS manifests that the degradation ways of LFX by CCF mainly consisted of decarboxylation, demethylation and ring-opening, etc. This work provides a novel approach for improving photocatalytic properties of g-C_3N_4 by constructing heterojunction coupled with CQDs induction strategy.

CRediT authorship contribution statement

Guohua Dong: Writing – original draft, Supervision, Funding acquisition, Conceptualization. **Ming Zhao:** Visualization, Software. **Liming Bai:** Software, Investigation. **Lijian Meng:** Validation, Software. **Dong-feng Chai:** Visualization, Methodology. **Wenzhi Zhang:** Validation, Supervision, Project administration. **Dongzhe Zhang:** Validation, Data curation. **Pengda Han:** Writing – original draft, Software, Data curation. **Yunuo Li:** Writing – review & editing, Writing – original draft, Data curation.

Acknowledgments

This work was supported by the National Natural Science Foundation of China (Grant No. 32272823), the Heilongjiang Provincial Natural Science Foundation of China (Grant No. PL2024C037), and the Research Foundation of Education Bureau of Heilongjiang Province of China (Grant No. 145309609). We also thank eceshi Lab (https://www.eceshi.com/) for the ESR analysis.

Declaration of Competing Interest

The authors declare that they have no known competing financial interests or personal relationships that could have appeared to influence the work reported in this paper.

Appendix A. Supporting information

Supplementary data associated with this article can be found in the online version at doi:10.1016/j.colsurfa.2025.138141.

Data Availability

Data will be made available on request.

References

[1] Z. Qiu, G. Shen, Z. Ruan, et al., Efficient removal of organic pollutants by metal–organic framework derived Co-N@C hollow multi-shell nanoreactors: size-exclusion and confinement effect, Chem. Eng. J. 511 (2025) 162227, https://doi.org/10.1016/j.cej.2025.162227.

[2] A. Singh, S.G. Pratap, A. Raj, Occurrence and dissemination of antibiotics and antibiotic resistance in aquatic environment and its ecological implications: a review, Environ. Sci. Pollut. Res. 31 (2024) 47505–47529, https://doi.org/10.1007/s11356-024-34355-x.

[3] H.-J. Zhu, Y.-K. Yang, M.-H. Li, et al., Photocatalytic in situ H_2O_2 production and activation for enhanced ciprofloxacin degradation over CeO_2-Co_3O_4/g-C_3N_4: key role of CeO_2, Rare Met 43 (2024) 2695–2707, https://doi.org/10.1007/s12598-023-02583-8.

[4] C. Zhang, L. Lin, M. Zhou, et al., Dual functional S-scheme $ZnIn_2S_4$/crystalline polymeric carbon nitride (ZIS/CPCN) heterojunction for efficient photocatalytic hydrogen evolution and degradation of levofloxacin, Chem. Eng. J. 495 (2024) 153563, https://doi.org/10.1016/j.cej.2024.153563.

[5] L. Jia, L.-M. Yang, W. Wang, et al., Preparation and characterization of Rb-doped TiO_2 powders for photocatalytic applications, Rare Met 43 (2024) 555–561, https://doi.org/10.1007/s12598-019-01241-2.

[6] P. Ranjit, V. Jhansi, K.V. Reddy, Conventional wastewater treatment processes, in: N.R. Maddela, L.C. García Cruzatty, S. Chakraborty (Eds.), Advances in the Domain of Environmental Biotechnology: Microbiological Developments in Industries, Wastewater Treatment and Agriculture, Springer, Singapore, Singapore, 2021, pp. 455–479.

[7] Y. Li, Y. Ma, Y. Jiang, et al., Core-shell structured Co/MnO@N-doped carbon efficiently generates non-radicals for water purification in Fenton-like catalysis, Sep. Purif. Technol. 354 (2025) 128993, https://doi.org/10.1016/j.seppur.2024.128993.

[8] Y. Chen, Y. Jingling, Z. Lixi, et al., Recent progress on the removal of antibiotic pollutants using photocatalytic oxidation process, Crit. Rev. Environ. Sci. Technol. 52 (2022) 1401–1448, https://doi.org/10.1080/10643389.2020.1859289.

[9] Z. Qiu, C. Chen, X. Zeng, et al., Redox-copolymer-enhanced electrochemical catalysis membrane for efficient water decontamination, Chem. Eng. J. 505 (2025) 159383, https://doi.org/10.1016/j.cej.2025.159383.

[10] L. Yang, R.P. Sivasankaran, M.K. Song, et al., Highly selective solar CO_2 conversion into formic acid in Nickel-Perylene-C_3N_4 semiconductor photocatalyst, Adv. Energy Mater. 15 (2024) 2402798, https://doi.org/10.1002/aenm.202402798.

[11] F. Yu, J. Gu, H. Hao, et al., Removal of levofloxacin by H_2O_2 and PMS co-activation by sulfide-supported oxalate zero-valent iron enhanced with simultaneous catalysis of $SO_4^{\bullet-}$ and $^1O_2$: major free radicals, synergistic effects and mechanism exploration, Sep. Purif. Technol. 354 (2025) 129486, https://doi.org/10.1016/j.seppur.2024.129486.

[12] Y. Deng, S. Wang, T. Zhou, et al., Highly-separated co anchored on S, O-doped carbon nitride for enhanced peroxymonosulfate activation: insights into radical and non-radical pathways, Chem. Eng. J. 497 (2024) 154580, https://doi.org/10.1016/j.cej.2024.154580.

[13] D. Lin, J. Li, R. Wu, et al., Engineering lattice strain in bimetallic nanostructures to modulate peroxymonosulfate activation pathways, Sep. Purif. Technol. 359 (2025) 130612, https://doi.org/10.1016/j.seppur.2024.130612.

[14] Z. Ruan, R. Wu, C. Fu, et al., Efficient peroxymonosulfate activation for practical wastewater treatment by Biochar-Iron oxide composite-based hydrogel beads, Chem. Eng. J. 500 (2024) 157226, https://doi.org/10.1016/j.cej.2024.157226.

[15] S. Feng, T. Xie, J. Wang, et al., Photocatalytic activation of PMS over magnetic heterojunction photocatalyst $SrTiO_3$/$BaFe_{12}O_{19}$ for tetracycline ultrafast degradation, Chem. Eng. J. 470 (2023) 143900, https://doi.org/10.1016/j.cej.2023.143900.

[16] C. Peng, Q. Wang, X. Zhang, et al., Efficient degradation of SCP by $Co_2(OH)_2CO_3$/$CuCo_2S_4$-enhanced electron transfer-activated PMS: dual role of cu active site, Sep. Purif. Technol. 362 (2025) 131738, https://doi.org/10.1016/j.seppur.2025.131738.

[17] J.M. Zhao, X.Y. Cao, Y.B. Bai, et al., Simple synthesis of $CaTiO_3$/g-C_3N_4 heterojunction for efficient photodegradation of methylene blue and levofloxacin, Opt. Mater. 135 (2023), https://doi.org/10.1016/j.optmat.2022.113239.

[18] J. Wen, J. Xie, X. Chen, et al., A review on g-C_3N_4-based photocatalysts, Appl. Surf. Sci. 391 (2017) 72–123, https://doi.org/10.1016/j.apsusc.2016.07.030.

[19] Y. Li, M. Zhou, B. Cheng, et al., Recent advances in g-C_3N_4-based heterojunction photocatalysts, J. Mater. Sci. Technol. 56 (2020) 1–17, https://doi.org/10.1016/j.jmst.2020.04.028.

[20] M.E. Khan, A. Mohammad, T. Yoon, State-of-the-art developments in carbon quantum dots (CQDs): Photo-catalysis, bio-imaging, and bio-sensing applications, Chemosphere 302 (2022) 134815, https://doi.org/10.1016/j.chemosphere.2022.134815.

[21] S.Y. Lim, W. Shen, Z. Gao, Carbon quantum dots and their applications, Chem. Soc. Rev. 44 (2015) 362–381, https://doi.org/10.1039/c4cs00269e.

[22] R. Das, R. Bandyopadhyay, P. Pramanik, Carbon quantum dots from natural resource: a review, Mater. Today Chem. 8 (2018) 96–109, https://doi.org/10.1016/j.mtchem.2018.03.003.

[23] A. Mei, Z. Xu, X. Wang, et al., Photocatalytic materials modified with carbon quantum dots for the degradation of organic pollutants under visible light: a review, Environ. Res. 214 (2022) 114160, https://doi.org/10.1016/j.envres.2022.114160.

[24] F. Zhao, X. Li, M. Zuo, et al., Preparation of photocatalysts decorated by carbon quantum dots (CQDs) and their applications: a review, J. Environ. Chem. Eng. 11 (2023) 109487, https://doi.org/10.1016/j.jece.2023.109487.

[25] N. Syed, J. Huang, Y. Feng, CQDs as emerging trends for future prospect in enhancement of photocatalytic activity, Carbon Lett. 32 (2022) 81–97, https://doi.org/10.1007/s42823-021-00282-x.

[26] P.-d Han, G.-h Dong, X.-j Zhang, et al., Microwave-assisted preparation of z scheme heterojunction by anchoring $ZnFe_2O_4$ on tubular-like g-C_3N_4 for peroxymonosulfate activation towards levofloxacin degradation, J. Cent. South Univ. 32 (2025) 894–918, https://doi.org/10.1007/s11771-025-5872-z.

[27] M.I. Yousaf, H. Mansha, U. Habiba, et al., Visible light active N, S-Carbon quantum dots@$FeVO_4$ nanocomposite as a photodegradation mechanism for wastewater treatment, Mater. Sci. Eng. B. 319 (2025) 118376, https://doi.org/10.1016/j.mseb.2025.118376.

[28] M.M. Sajid, N.A. Shad, Y. Javed, et al., Morphological effects on the photocatalytic performance of $FeVO_4$ nanocomposite, NanoStruct. Nano-Objects (2020) 100431, https://doi.org/10.1016/j.nanoso.2020.100431.

[29] T. Alomayri, Enhanced interfacial charge transfer in $BiVO_4$/rGO/$FeVO_4$ heterojunction composite for improved photocatalysis water purification, Ceram. Int. 51 (2025) 10193–10199, https://doi.org/10.1016/j.ceramint.2024.12.450.

[30] S. Majumder, A.A. Yadav, Y.M. Hunge, et al., Exploring $FeVO_4$/$ZnCo_2O_4$ n-p heterojunctions for superior photoelectrochemical performance, J. Alloy. Compd. 1010 (2025) 177281, https://doi.org/10.1016/j.jallcom.2024.177281.

[31] X. Guo, Y. Xi, Y. Li, et al., Ag regulates the interfacial electric field of g-C_3N_4/$FeVO_4$ S-scheme heterojunction for activated H_2O_2 degradation of organic pollutants in complex environments, Chem. Eng. J. 505 (2025) 159640, https://doi.org/10.1016/j.cej.2025.159640.

[32] T. Jin, C. Liu, F. Chen, et al., Synthesis of g-C_3N_4/CQDs composite and its photocatalytic degradation property for rhodamine b, Carbon Lett. 32 (2022) 1451–1462, https://doi.org/10.1007/s42823-022-00382-2.

[33] J. Li, W. Zhao, Y. Guo, et al., Facile synthesis and high activity of novel $BiVO_4$/$FeVO_4$ heterojunction photocatalyst for degradation of metronidazole, Appl. Surf. Sci. 351 (2015) 270–279, https://doi.org/10.1016/j.apsusc.2015.05.134.

[34] Y.-C. Shen, D.R. Sahu, J.-L. Huang, et al., Synthesis and performance enhancement of Ni–Mo/g-C_3N_4 bimetallic composites electrocatalysts, Mater. Sci. Semicond. Process 195 (2025) 109625, https://doi.org/10.1016/j.mssp.2025.109625.

[35] H. Wang, W. He, Xa Dong, et al., In situ FT-IR investigation on the reaction mechanism of visible light photocatalytic NO oxidation with defective g-C_3N_4, Sci. Bull. 63 (2018) 117–125, https://doi.org/10.1016/j.scib.2017.12.013.

[36] K.P. Thaba, M.M. Mphahlele-Makgwane, P.I. Kyesmen, et al., Composition-dependent structure evolution of $FeVO_4$ nano-oxide and its visible-light photocatalytic activity for degradation of methylene blue, Colloids Surf. Physicochem. Eng. Asp. 633 (2022) 127856, https://doi.org/10.1016/j.colsurfa.2021.127856.

[37] H. Sun, P. Wu, Tuning the functional groups of carbon quantum dots in thin film nanocomposite membranes for nanofiltration, J. Membr. Sci. 564 (2018) 394–403, https://doi.org/10.1016/j.memsci.2018.07.044.

[38] S. Zhang, X. Li, K. Li, et al., A controllable one-step millisecond synthesis of nanocrystalline mesoporous MgO with template-free by gliding arc plasma for efficient photocatalytic degradation of organic compounds, J. Mater. Sci. Technol. 230 (2025) 195–204, https://doi.org/10.1016/j.jmst.2025.01.024.

[39] N.Q. Tung, D.T.C. Van, D.X. Thang, et al., Hydrothermal synthesis of CuCoFe layered double hydroxide and its performance in the degradation of antibiotics: influencing factors, degradation pathways, and reaction mechanism, J. Environ. Chem. Eng. 11 (2023) 110127, https://doi.org/10.1016/j.jece.2023.110127.

[40] L. Liu, R. Zhan, M. Zhang, et al., Insights into the performance, mechanism, and ecotoxicity of levofloxacin degradation in $CoFe_2O_4$ catalytic peroxymonosulfate

process, J. Environ. Chem. Eng. 10 (2022) 107435, https://doi.org/10.1016/j.jece.2022.107435.
[41] M. Kohantorabi, G. Moussavi, S. Giannakis, A review of the innovations in metal- and carbon-based catalysts explored for heterogeneous peroxymonosulfate (PMS) activation, with focus on radical vs. Non-radical degradation pathways of organic contaminants, Chem. Eng. J. 411 (2021) 127957, https://doi.org/10.1016/j.cej.2020.127957.
[42] T.T.B. Huyen, N.T.C. Tien, N.T.G. Huy, et al., Fe-modified ZnO for enhancing the photocatalytic removal of levofloxacin in water via persulfate activation, Eng. Res. Express 7 (2025), https://doi.org/10.1088/2631-8695/adc5c6.
[43] C.-C. Wang, F.-S. Shieu, H.C. Shih, Ag-nanoparticle enhanced photodegradation of ZnO nanostructures: investigation using photoluminescence and ESR studies, J. Environ. Chem. Eng. 9 (2021) 104707, https://doi.org/10.1016/j.jece.2020.104707.
[44] M. Yang, R. Li, H. Xu, et al., Interface-Transferring electrons and photogenerated carriers in $W_{18}O_{49}$/N-Doped c to boost photothermocatalytic ethanol dehydration to ethylene, ACS Sustain. Chem. Eng. 13 (2025) 4211–4221, https://doi.org/10.1021/acssuschemeng.4c10687.
[45] H. Jung, A. Jamal, I. Gereige, et al., Continuous flow photoelectrochemical reactor with gas permeable photocathode: enhanced photocurrent and partial current density for CO_2 reduction, Adv. Sci. 12 (2024), https://doi.org/10.1002/advs.202411348.
[46] N.V.N. Mai, T.T.T. Phuong, N.V. Luong, et al., Enhanced photodegradation ability of antibiotics with composite based on V_2O_5 under visible light, VNU Journal Science Natural Sciences Technology (2025), https://doi.org/10.25073/2588-1140/vnunst.5617.
[47] C. Luo, Y. Xie, S. Huang, et al., Synergetic oxygen vacancy and homologous heterojunction into BiOCl/$Bi_2Fe_4O_9$ for levofloxacin photodegradation: insight of Ov-O*-PMS intermediate toward efficient $^1O_2$ generation, Sep. Purif. Technol. 375 (2025) 133854, https://doi.org/10.1016/j.seppur.2025.133854.
[48] S.L. Prabavathi, K. Saravanakumar, C.M. Park, et al., Photocatalytic degradation of levofloxacin by a novel Sm_6WO_{12}/g-C_3N_4 heterojunction: performance, mechanism and degradation pathways, Sep. Purif. Technol. 257 (2021) 117985, https://doi.org/10.1016/j.seppur.2020.117985.
[49] Y. Zhao, H. Guo, J. Liu, et al., Effective photodegradation of rhodamine b and levofloxacin over CQDs modified BiOCl and BiOBr composite: mechanism and toxicity assessment, J. Colloid Interface Sci. 627 (2022) 180–193, https://doi.org/10.1016/j.jcis.2022.07.046.
[50] B. Wang, C. Wang, Y. Tang, et al., High-efficiency photodegradation of levofloxacin enabled by hybrid Ag_2MoO_4@AgCl composites: performance, pathways, and mechanism insight, Appl. Surf. Sci. 697 (2025) 162970, https://doi.org/10.1016/j.apsusc.2025.162970.